SCIENCE CHINA
Chemistry

•ARTICLES•

June 2022 Vol.65 No.6: 1157–1163
https://doi.org/10.1007/s11426-022-1247-1

# Over 16% efficiency all-polymer solar cells by sequential deposition

Bangbang Li[1], Xuanyu Zhang[3], Ziang Wu[4], Jie Yang[1], Bin Liu[1], Qiaogan Liao[1,2], Junwei Wang[1], Kui Feng[1], Rui Chen[3], Han Young Woo[4], Fei Ye[1], Li Niu[2], Xugang Guo[1,5] & Huiliang Sun[1,2*]

[1]*Department of Materials Science and Engineering, Southern University of Science and Technology (SUSTech), Shenzhen 518055, China;*
[2]*Center for Advanced Analytical Science, School of Chemistry and Chemical Engineering, Guangzhou University, Guangzhou 510006, China;*
[3]*Department of Electrical and Electronic Engineering, Southern University of Science and Technology (SUSTech), Shenzhen 518055, China;*
[4]*Department of Chemistry, Korea University, Seoul 136-713, Republic of Korea;*
[5]*Guangdong Provincial Key Laboratory of Functional Oxide Materials and Devices, SUSTech, Shenzhen 518055, China*

Received February 26, 2022; accepted April 6, 2022; published online May 10, 2022

All-polymer solar cells (all-PSCs) have received extensive attention due to their excellent mechanical robustness and performance stability. However, the power conversion efficiency (PCE) of all-PSCs still lags behind those of organic solar cells (OSCs) based on non-fullerene small molecule acceptors. Herein, we report highly efficient all-PSCs *via* sequential deposition (SD) with donor and acceptor layers coated sequentially to optimize the film microstructure. Compared with the bulk heterojunction (BHJ) all-PSCs, an optimized morphology with vertical component distribution was achieved for the SD-processed all-PSCs due to the synergistic effect of swelling of polymer films and using additive. Such strategy involves using chlorobenzene as the first layer processing-solvent for polymer donor, chloroform as the second processing-solvent for polymer acceptor with trace 1-chloronaphthalene, efficiently promoting exciton dissociation and charge extraction and reducing trap-assisted recombination. Consequently, over 16% all-PSCs fabricated *via* SD method was realized for the first time, which is much higher than that (15.2%) of its BHJ counterpart and also among the highest PCEs in all-PSCs. We have further demonstrated the generality of this approach in various all-polymer systems. This work indicates that the SD method can yield excellent all-PSCs and provides a facile approach to fabricating high-performance all-PSCs.

**all-polymer solar cells, polymer acceptors, planar heterojunction, sequential deposition**

**Citation:** Li B, Zhang X, Wu Z, Yang J, Liu B, Liao Q, Wang J, Feng K, Chen R, Woo HY, Ye F, Niu L, Guo X, Sun H. Over 16% efficiency all-polymer solar cells by sequential deposition. *Sci China Chem*, 2022, 65: 1157–1163, https://doi.org/10.1007/s11426-022-1247-1

## 1 Introduction

As a clean and renewable energy conversion device, organic solar cells (OSCs) have received extensive attention from the academic and industrial community benefiting from the advantages such as processability, lightweight, and low cost [1–5]. Among various OSCs, all-polymer solar cells (all-PSCs) based on the combination of polymer donors and polymer acceptors show unique merits including superior stability and mechanical robustness [6–10]. Recently, polymerized small molecule acceptors (SMAs) have boosted the power conversion efficiency (PCE) of all-PSCs over 14% by rational material design and device optimization [11–16]. However, there is still a large gap in terms of PCEs between all-PSCs and polymer:SMAs-based OSCs [17,18]. One of the most important reasons is that it is difficult to achieve nanoscale phase separation for bulk heterojunction (BHJ) dominant structure in all-PSCs [19–21]. Although various morphology control strategies from the molecular design and device optimization have been implemented, controlling the

*Corresponding author (email: huiliang@gzhu.edu.cn)

side-chain entanglement and backbone orientation to achieve sophisticated film microstructure, especially the distribution of the polymer donor and polymer acceptor in the vertical direction in BHJ all-PSCs, still remains a challenge.

Compared with the BHJ structure, the pseudo-planar heterojunction (or layer-by-layer, LBL) configuration is fabricated by the sequential deposition (SD) method, in which the donor and acceptor layers are prepared separately [22]. Such a method not only can manipulate and optimize the microstructure of donor and acceptor layers independently but also overcome the drawbacks induced by intrinsic material properties, giving extrinsic advantages in control of vertical phase distribution [23–28]. Although the SD method has recently achieved great success in OSCs based on polymer:SMAs systems, there are few reports on high-performance LBL all-PSCs *via* the SD method due to the polymer similar solubility [29–31]. For instance, despite the fact that the LBL structures achieved a more suitable morphology than the BHJ ones, the highest PCEs of LBL all-PSCs based on the classic naphthalene diimide (NDI) and perylene diimide (PDI) polymers is less than 10% [32–34]. In addition, polymerized SMAs have been proven to be an effective strategy for improving the device performance in BHJ all-PSCs. Despite this, there are only a few successful examples in LBL all-PSCs [15,26,32].

Inspired by the great success of SD mothed for OSCs based on polymer:SMA blends and polymerized SMAs for improving PCEs of all-PSCs, herein, we report a high-performance SD-processed LBL all-PSCs based on polymer donor PM6 and polymer acceptor L15 (Figure 1a). During the SD process, chlorobenzene (CB) was used as the first processing solvent for PM6, while non-orthogonal solvent chloroform (CF) was used as the second processing solvent for L15 with trace 1-chloronaphthalene (CN). Our SD method enabled favorable vertical phase separation and ordered molecular packing for all-polymer systems. In addition,

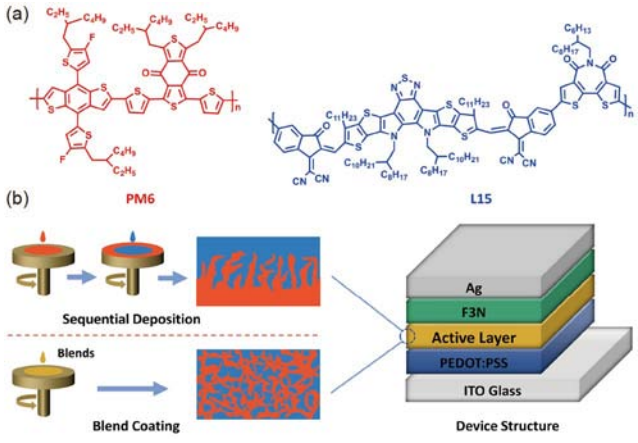


**Figure 1** (a) Molecular structures of PM6 and L15; (b) the two processing methods of active layer fabricated by spin-coating and the convention OSC device structure (color online).

optical characterization shows that LBL all-PSCs have better light absorption and more balanced carrier transport than those of BHJ all-PSCs. Moreover, the results of femtosecond transient absorption (TA) spectra and light-intensity dependencies data demonstrate that LBL all-PSCs exhibit efficient exciton dissociation at the donor/acceptor interface, swift charge extraction, and reduced bimolecular recombination. As a result, the optimized all-PSCs show an excellent PCE of 16.15%, which is the best value among the SD-processed all-PSCs to date and which is also much higher than that (15.19%) of the corresponding BHJ counterpart. Of particular note is that our SD method also has certain general applicability, which is reflected in the performance improvement in the other three all-polymer systems.

## 2 Results and discussion

The chemical structures of PM6 and L15 are shown in Figure 1a. The measured $M_n$ values of PM6 and L15 were 32.2 and 22.2 kDa, with dispersity values of 1.9 and 2.2, respectively [12,35]. L15 was synthesized based on our previous work [12,13]. All-PSCs were fabricated using a conventional configuration (Figure 1b). The LBL film was sequentially cast independently using a solution in CB of PM6 and a solution in CF of L15 with trace additive. In such the SD process, the CF solvent quickly evaporated and spread into a film under high-speed spin-coating. The corresponding BHJ film was fabricated by blend coating (BC) method, spin-coating from a CF solution of mixed PM6 and L15 with trace additive. See Supporting Information online for the detailed device optimization process and the corresponding photovoltaic parameters.

The current density-voltage (*J*-*V*) test curves of LBL and BHJ all-PSCs under optimal conditions are shown in Figure 2a. It is found that the LBL all-PSC with a content of 2% CN yields the highest PCE of 16.15%, with a short-currents density ($J_{sc}$) of 23.58 mA cm$^{-2}$, fill factor (FF) of 73.17% and an open-circuit voltage ($V_{oc}$) of 0.936 V, which is higher its BHJ counterpart with a PCE of 15.19% (the $J_{sc}$ is 22.51 mA cm$^{-2}$, the FF is 71.31%, and the $V_{oc}$ is 0.946 V) (Table 1). The integrating currents from the external quantum efficiency (EQE) measurement are 22.73 and 21.69 mA cm$^{-2}$ for LBL and BHJ devices, respectively (Figure 2b), which is consistent with the above measured $J_{sc}$. The efficiency distributions of fifteen sets of optimized LBL and BHJ devices are shown in Figure 2c, which both exhibit a normal distribution. The average PCE value of the LBL device is 15.59%, which is much higher than that (14.66%) of BHJ devices. To the best of our knowledge, the 16.15% efficiency is among the highest values reported so far for all-PSCs (as shown in Figure 2d and Table S11, Supporting Information online).

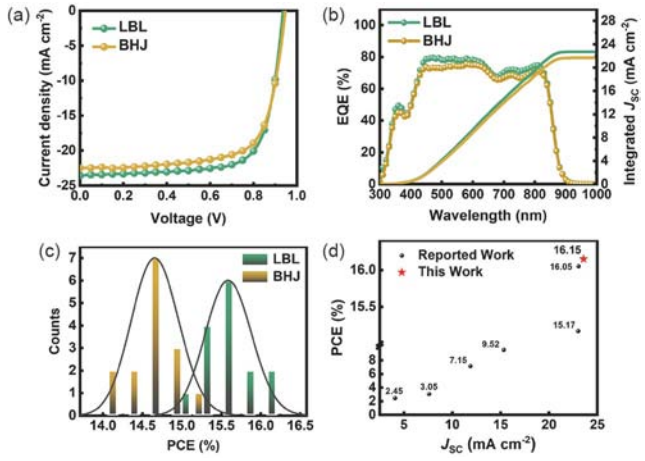


**Figure 2** (a) The optimized *J*-*V* curves of BHJ and LBL all-PSCs; (b) the EQE and integral $J_{sc}$ tested under the optimal PCE; (c) histograms of the PCE counts of BHJ and LBL devices for 15 individual devices; (d) plots of the PCE *versus* FF for the representative LBL all-PSCs reported in the literature, the PCE is almost below 16% except for one example reported during the reviewing process of this work [15] (color online).

To visually understand the differences in device performance of BHJ and LBL all-PSCs from physical dynamics [24,36], we studied the influence of the SD method on the active layer morphology by atomic force microscopy (AFM) and transmission electron microscopy (TEM). As shown in Figure 3a, b, the surface of the LBL film fabricated under optimal condition is greatly coarser than the corresponding BHJ film, with root-mean-square (RMS) values of 2.74 and 1.64 nm, respectively. It is speculated that the SD method facilitates phase separation between donor and acceptor layers due to the enhanced crystallization of L15 by CN additive. As can be seen from the TEM images of Figure 3c, d, the LBL film at the 200 and 500 nm scale exhibited larger and well-defined fibre-like networks than those of BHJ film, indicating SD method optimized phase distribution between donor and acceptor layers. Then, we carried out 2D grazing-incidence wide-angle X-ray scattering (GIWAXS) measurements to further study the characteristics of the film molecular packing and crystallinity [26,37–39]. The 2D-GIWAXS diffraction patterns and 1D line-out profiles of the neat films of PM6 and L15 are shown in Table S9 and Figure S10 (Supporting Information online). The neat PM6 film shows a strong (100) peak at 0.292 Å$^{-1}$ (*d*=21.518 Å) in the in-plane (IP) direction and a weak (010) peak at 1.661 Å$^{-1}$ (*d* =3.783 Å) in the out-of-plane (OOP) direction. The neat L15 film shows a strong π-π stacking peak in the OOP direction, as evidenced by the strong (010) lamellar peaks at 1.602 Å$^{-1}$ (*d*=3.922 Å), indicating a face-on dominant orientation of L15. Moreover, the optimized LBL and BHJ film (Figure 3e, f) both show a strong diffraction peak in the OOP direction at 1.633 Å$^{-1}$ (*d*=3.848 Å), implying that the backbone ordering of L15 is maintained in the BHJ and LBL films. That is beneficial for charge transport in the vertical direction. In the IP direction, the scattering peak of both LBL and BHJ films at *q*=0.638 Å$^{-1}$ (*d*=9.848 Å) could be assigned to the lamellar stacking of either PM6 or L15. Additionally, the crystal coherence lengths (CCL) in the IP and OOP directions are calculated by the Scherrer equation. Both LBL and BHJ films have comparable CCL values. Moreover, the (100) signal intensity calculated by integrating the azimuthal curve (Figure S10j) shows that although the two films both show predominantly face-on orientation, a higher face-on/edge-on ratio (the face-on/edge-on ratio is 0.58 for the BHJ blend film and 0.72 for the LBL film) in the LBL film, contributing to the improved vertical charge transport, as evidenced by the SCLC measurements.

Next, we analyzed the reasons for the high performance of the LBL device from the working principle of OSCs, including exciton generation, exciton diffusion, exciton association, and charge extraction. First, we measured the optical properties of the optimized BHJ and LBL films to figure out the improvement of $J_{sc}$ in the LBL device from the aspect of exciton generation. The absorption spectrum demonstrates that PM6 has a strong absorption band in the visible light region, complementing that of the L15 film with strong absorption concentrated in the near-infrared region (Figure S2). This is conducive to the absorption of more photons from the sun. In addition, we find that the absorption coefficients of LBL and BHJ films in the visible region are basically the same, as high as $7.54\times10^4$ cm$^{-1}$ (Figure 4a). However, the absorption coefficient of LBL film is higher than that of BHJ film in the near-infrared region at around 808 nm, which indicates that LBL film prepared by the SD method promotes better light-harvesting, thereby significantly increasing the $J_{sc}$.

For further investigation of exciton generation and exciton diffusion dynamics of BHJ and LBL films, TA spectroscopy [40,41] was performed to characterize photo-to-electron conversion processes between donor and acceptor. As shown in Figure 4b, c and Figure S4a, we obtained 2D color plots of

**Table 1** Collection of photovoltaic parameters for BHJ and LBL device

| Devices [a] | D | A | $V_{oc}$ (V) | FF (%) | $J_{sc}$ (mA cm$^{-2}$) | Cal. $J_{sc}$/EQE (mA cm$^{-2}$) | PCE [b] (%) |
|---|---|---|---|---|---|---|---|
| | Addictive | | | | | | |
| BHJ | 2%CN | | 0.95 | 71.31 | 22.51 | 21.69 | 15.19(14.76) |
| LBL | w/o | 2% CN | 0.94 | 73.17 | 23.58 | 22.73 | 16.15(15.70) |

a) The device area: 4.5 mm$^2$; b) Average values with standard deviation from at least 10 devices.

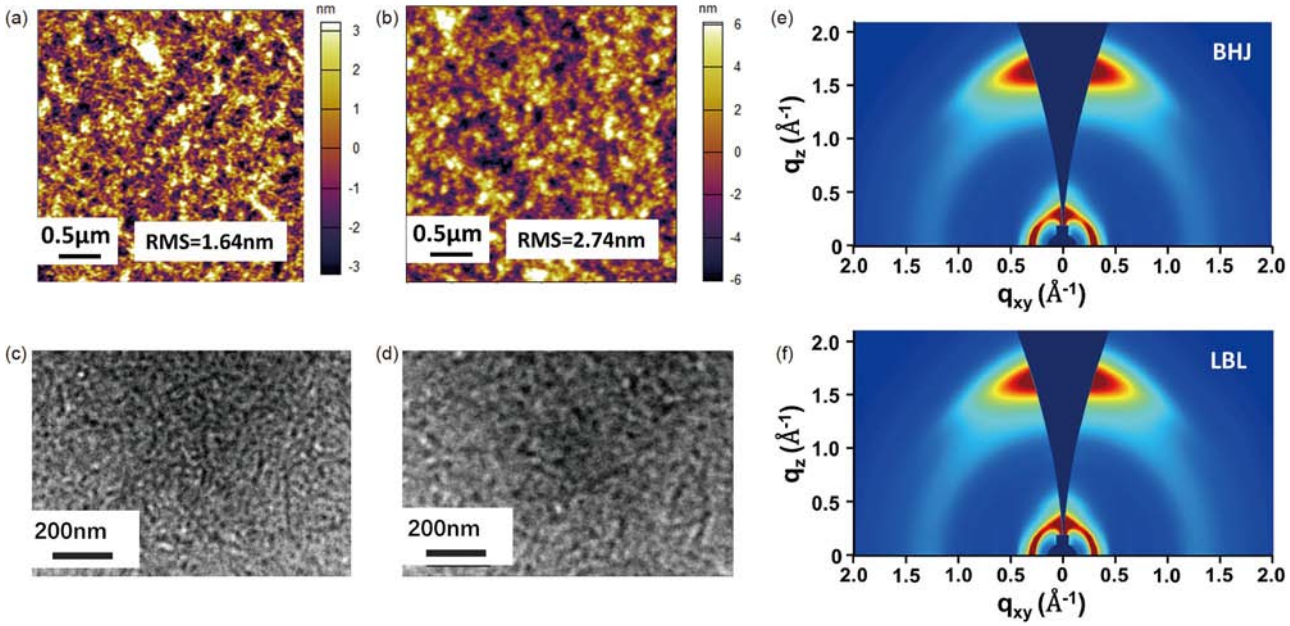


**Figure 3** AFM images of BHJ film (a) and LBL film (b); TEM images of BHJ film (c) and LBL film (d) at 200 nm; 2D-GIWAXS diffraction patterns of BHJ film (e) and LBL film (f) (color online).

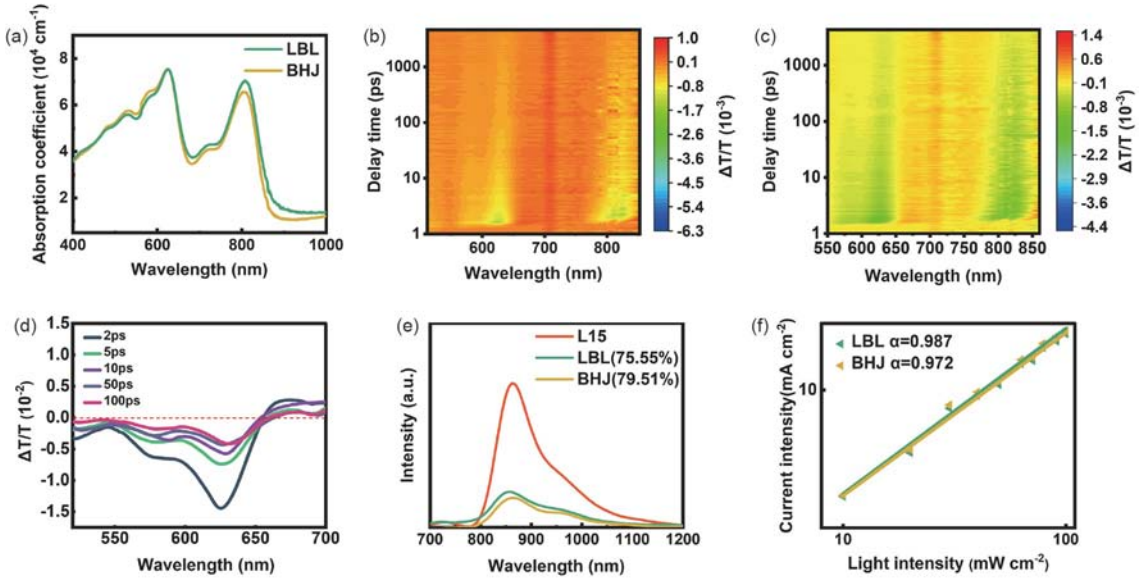


**Figure 4** (a) Absorption coefficient of the optimized BHJ and LBL active layer films; the 2D color plot of TA spectrum of BHJ film (b) and LBL film (c) at indicated delay times; (d) representative spectrum of LBL film at indicated delay times; (e) fitting PL spectrum of neat L15, LBL, and BHJ films; (f) current intensity plotted against incident light intensity for BHJ and LBL devices on a logarithmic scale (color online).

PM6, BHJ, and LBL films by a 355-nm pump pulse photo-excitation. There are two bleach peaks at around 625 and 820 nm in the TA spectrum of both BHJ and LBL films, separately attributed to the sum of ground state bleach (GSB) and stimulated emission (SE) of PM6 and L15. This result is consistent with the location of the absorption peak of PM6 and L15. Here, a few representative line-out profiles of LBL films from the TA spectrum are selected to probe the relative transmittance change ($\Delta T/T$) at specific delay times (Figure 4d). The GSB signal attenuation speed of the first 10 ps is much fast in contrast with the varies of that from 10 to 100 ps, which indicates that there is the hole transfer (HT) process. Thus, time-resolved photoluminescence (TRPL) spectroscopy [23,26] was employed to investigate the HT kinetics of BHJ and LBL films. The obtained plots at 582 nm were fitted by a biexponential function [42]: $i=A_1\exp(-t/\tau_1)+A_2\exp(-t/\tau_2)$, with pre-factors of $A_1$ and $A_2$ and two lifetimes of $\tau_1$ and $\tau_2$. Of note is that HT process consists of an ultrafast

dissociation of excitons at the donor/acceptor interface and a diffusion process of excitons to the donor/acceptor interface, as characterized by $\tau_1$ and $\tau_2$, respectively. Finally, biexponential fitting yields $\tau_1$=0.22/0.44 ps and $\tau_2$=34.53/56.66 ps for BHJ and LBL films (Figure S5 and Table S7), indicating LBL film is favorable for much exciton generation and efficient exciton diffusion in the whole HT process to achieve a high-performance device [42–44].

We also carried out photoluminescence (PL) spectra to reveal the efficiency of exciton dissociation between polymer donor and polymer acceptor [25]. As shown in Figure 4e, the neat L15 film shows a strong PL intensity in the range of 800–1,100 nm, but the intensity substantially decreases after the joining of PM6, which indicates efficient exciton dissociation and charge transfer occur at the donor/acceptor interface. We assessed the quenching efficiencies (ΔPL) of BHJ and LBL films using the equation [45]: $\Delta PL=(PL_{pristine}-PL_{HTL})/PL_{pristine}$, in which $PL_{pristine}$ is the PL peak value of L15, $PL_{HTL}$ approximately denotes the corresponding PL intensity of BHJ or LBL films. The calculated quenching efficiencies of BHJ and LBL films are 79.51% and 75.55%, respectively. It indicates more electrons dissociation and extraction in LBL film. The charge transport ability of BHJ and LBL devices is measured by the space-charge limited current (SCLC) technology [46]. As shown in Table S8, the calculated electron mobility ($\mu_e$) and hole mobility ($\mu_h$) results for LBL devices are $1.75\times10^{-4}$ and $1.7\times10^{-4}$ $cm^2\ V^{-1}\ s^{-1}$, respectively. The calculated results of the $\mu_e$ and $\mu_h$ for the BHJ device are $1.56\times10^{-4}$ and $1.67\times10^{-4}$ $cm^2\ V^{-1}\ s^{-1}$, respectively. On one hand, the $\mu_e$ and $\mu_h$ of LBL device are higher than those of BHJ device. On the other hand, in terms of the ratio of $\mu_e/\mu_h$, LBL device is closer to value 1 compared with the BHJ device. Thus, the transportation of electrons and holes in the LBL device is more efficient and balanced in the photovoltaic power generation process and corresponds to higher $J_{sc}$ and FF. In addition, light-intensity dependencies measurements were performed for investigating charge recombination in both LBL and BHJ devices [47].

Light intensity ($P$) and $J_{sc}$ follow the proportional relationship of $J_{sc} \propto P^{\alpha}$. Unless there is no bimolecular recombination for $\alpha$=1, $\alpha$ should be <1 for the devices due to bimolecular recombination in most cases [48]. As shown in Figure 4(f), the $\alpha$ values of LBL and BHJ devices are 0.987 and 0.972, respectively. It indicates that the reduced bimolecular recombination and swift charge extraction were achieved in the LBL device due to the optimized distribution between donor and acceptor layers.

To demonstrate the generality of our SD method, several other all-polymer systems based on PBDB-T:L15, PCE10:f-BTI3-T, and PBDB-T:N2200 blends were here chosen and the corresponding molecular structures were shown in Figure 5a, b. It was found that the LBL device based on PBDB-T:L15 achieved a PCE of 8.4%, which is much higher than that (6.5%) of the BHJ device (Figure 5c, e, Table 2). Similar results were also observed in the classical fused imide polymer acceptors-based two all-PSCs. However, the limited popularization of this method in several high-performance polymer:SMAs-based OSCs was also observed in Table S4.

## 3 Conclusions

We reported highly efficient all-PSCs using the SD method.

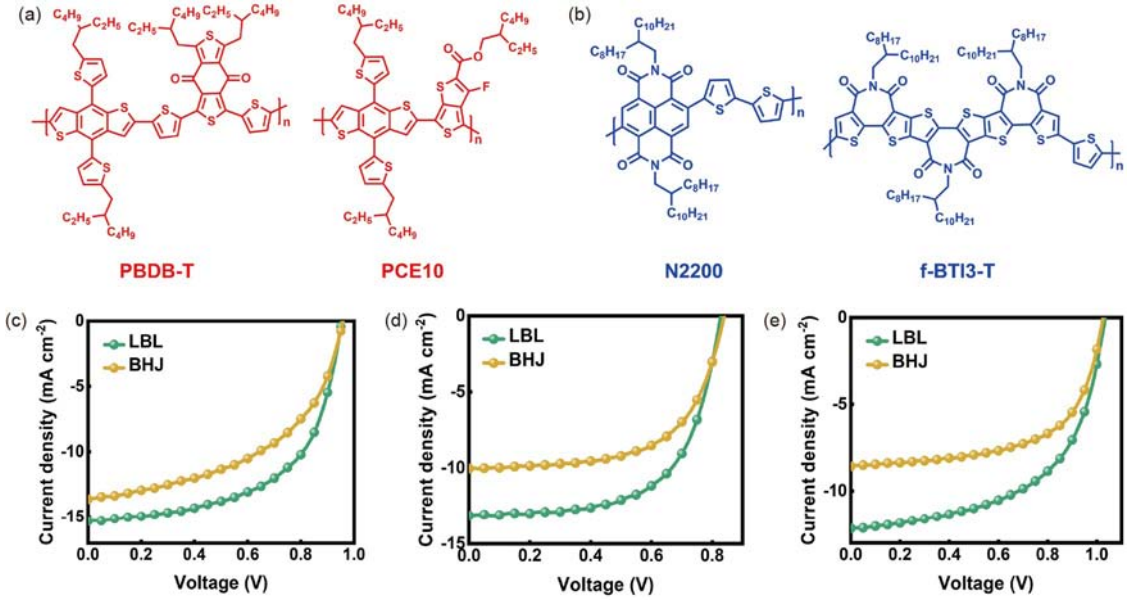


**Figure 5** Chemical structures of the classic polymer donors (a) and polymer acceptors (b). The *J-V* curves of PBDB-T:L15 (c), PBDB-T:N2200 (d), and PCE10:f-BTI3-T-based all-PSCs (e) (color online).

**Table 2** Summary of photovoltaic parameters for three representative all-PSCs systems prepared by SD and BC methods

| Devices | $V_{oc}$ (V) | $J_{sc}$ (mA cm$^{-2}$) | FF (%) | PCE (%) |
|---|---|---|---|---|
| PBDB-T/N2200 | 0.83 | 13.14 | 62.11 | 6.76 |
| PBDB-T:N2200 | 0.84 | 10.03 | 61.24 | 5.16 |
| PCE10/f-BTI3-T | 1.03 | 12.17 | 56.40 | 7.10 |
| PCE10:f-BTI3-T | 1.03 | 8.56 | 60.86 | 5.34 |
| PBDB-T/L15 | 0.95 | 15.30 | 57.84 | 8.43 |
| PBDB-T:L15 | 0.96 | 13.63 | 50.00 | 6.53 |

The non-orthogonal solvent used in fabrication and CN additive introduced in the neat L15 solution played a key role in manipulating overall layer morphology. Detailed investigations revealed that our SD method could offer better phase morphology than the typical BC method for all-polymer systems, thus improving carrier transport and generation and suppressing charge recombination. Consequently, these enhanced $J_{sc}$ and FF for the resulting all-PSCs. The optimal all-PSCs yield a remarkable PCE of 16.15% (the highest for LBL all-PSCs), outperforming the control devices (15.2%). The general applicability of the SD method to the other three all-polymer systems has also been demonstrated to deliver higher PCEs than their BHJ counterparts. Our SD method provides an avenue to highly efficient all-PSCs and profound enlightenment in the further construction of high-performance photovoltaic devices.

**Acknowledgements** This work was supported by the National Natural Science Foundation of China (52173172, 52173171, 21774055), the Natural Science Foundation for Distinguished Young Scholars of Guangdong Province (2021B1515020027), the Shenzhen Science and Technology Innovation Commission (JCYJ20210324310481303 5, JCYJ20180504165709042), the Open Fund of the State Key Laboratory of Luminescent Materials and Devices (South China University of Technology) and China Postdoctoral Science Foundation (2021M700062). H.Y. Woo is grateful for the financial support from the Natural Research Foundation of Korea (2016M1A2A2940911, 2015M1A2A2057506). We acknowledge the support of the Guangdong Provincial Key Laboratory Program (2021B1212040001) from the Department of Science and Technology of Guangdong Province. We thank Dr Yinhua Yang, Hua Li, and Lin Lin at the Materials Characterization and Preparation Center SUSTech for the high temperature NMR and HRMS testing, respectively. Our work was also supported by the Center for Computational Science and Engineering of SUSTech.

**Conflict of interest** The authors declare no conflict of interest.

**Supporting information** The supporting information is available online at http://chem.scichina.com and http://link.springer.com/journal/11426. The supporting materials are published as submitted, without typesetting or editing. The responsibility for scientific accuracy and content remains entirely with the authors.

1 Lin Y, Wang J, Zhang ZG, Bai H, Li Y, Zhu D, Zhan X. *Adv Mater*, 2015, 27: 1170–1174
2 Hou J, Inganäs O, Friend RH, Gao F. *Nat Mater*, 2018, 17: 119–128
3 Ji X, Xiao Z, Sun H, Guo X, Ding L. *J Semicond*, 2021, 42: 080202
4 Yang M, Wei W, Zhou X, Wang Z, Duan C. *Energy Mater*, 2021, 1: 100008
5 Liu Y, Liu B, Ma CQ, Huang F, Feng G, Chen H, Hou J, Yan L, Wei Q, Luo Q, Bao Q, Ma W, Liu W, Li W, Wan X, Hu X, Han Y, Li Y, Zhou Y, Zou Y, Chen Y, Li Y, Chen Y, Tang Z, Hu Z, Zhang ZG, Bo Z. *Sci China Chem*, 2022, 65: 224–268
6 Lee J, Sun C, Ma BS, Kim HJ, Wang C, Ryu JM, Lim C, Kim T, Kim Y, Kwon S, Kim BJ. *Adv Energy Mater*, 2021, 11: 2003367
7 Lee C, Lee S, Kim GU, Lee W, Kim BJ. *Chem Rev*, 2019, 119: 8028–8086
8 Wu B, Yin B, Duan C, Ding L. *J Semicond*, 2021, 42: 080301
9 Duan C, Ding L. *Sci Bull*, 2020, 65: 1508–1510
10 Ma R, Zhou K, Sun Y, Liu T, Kan Y, Xiao Y, Dela Peña TA, Li Y, Zou X, Xing Z, Luo Z, Wong KS, Lu X, Ye L, Yan H, Gao K. *Matter*, 2022, 5: 725–734
11 Zhang ZG, Li Y. *Angew Chem Int Ed*, 2021, 60: 4422–4433
12 Sun H, Liu B, Ma Y, Lee JW, Yang J, Wang J, Li Y, Li B, Feng K, Shi Y, Zhang B, Han D, Meng H, Niu L, Kim BJ, Zheng Q, Guo X. *Adv Mater*, 2021, 33: 2102635
13 Sun H, Yu H, Shi Y, Yu J, Peng Z, Zhang X, Liu B, Wang J, Singh R, Lee J, Li Y, Wei Z, Liao Q, Kan Z, Ye L, Yan H, Gao F, Guo X. *Adv Mater*, 2020, 32: 2004183
14 Sun R, Wang W, Yu H, Chen Z, Xia XX, Shen H, Guo J, Shi M, Zheng Y, Wu Y, Yang W, Wang T, Wu Q, Yang YM, Lu X, Xia J, Brabec CJ, Yan H, Li Y, Min J. *Joule*, 2021, 5: 1548–1565
15 Zhang Y, Wu B, He Y, Deng W, Li J, Li J, Qiao N, Xing Y, Yuan X, Li N, Brabec CJ, Wu H, Lu G, Duan C, Huang F, Cao Y. *Nano Energy*, 2022, 93: 106858
16 Sun C, Lee J, Seo S, Lee S, Wang C, Li H, Tan Z, Kwon S, Kim BJ, Kim Y. *Adv Energy Mater*, 2022, 12: 2103239
17 Cai Y, Li Y, Wang R, Wu H, Chen Z, Zhang J, Ma Z, Hao X, Zhao Y, Zhang C, Huang F, Sun Y. *Adv Mater*, 2021, 33: 2101733
18 Hong L, Yao H, Cui Y, Bi P, Zhang T, Cheng Y, Zu Y, Qin J, Yu R, Ge Z, Hou J. *Adv Mater*, 2021, 33: 2103091
19 Zhu L, Zhong W, Qiu C, Lyu B, Zhou Z, Zhang M, Song J, Xu J, Wang J, Ali J, Feng W, Shi Z, Gu X, Ying L, Zhang Y, Liu F. *Adv Mater*, 2019, 31: 1902899
20 Zou Y, Ye L. *Chem*, 2021, 7: 2853–2854
21 Zhou K, Liu Y, Alotaibi A, Yuan J, Jiang C, Xin J, Liu X, Collins BA, Zhang F, Ma W. *ACS Energy Lett*, 2020, 5: 589–596
22 Cui Y, Zhang S, Liang N, Kong J, Yang C, Yao H, Ma L, Hou J. *Adv Mater*, 2018, 30: 1802499
23 Chen H, Zhao T, Li L, Tan P, Lai H, Zhu Y, Lai X, Han L, Zheng N, Guo L, He F. *Adv Mater*, 2021, 33: 2102778
24 Wei Y, Yu J, Qin L, Chen H, Wu X, Wei Z, Zhang X, Xiao Z, Ding L, Gao F, Huang H. *Energy Environ Sci*, 2021, 14: 2314–2321
25 Weng K, Ye L, Zhu L, Xu J, Zhou J, Feng X, Lu G, Tan S, Liu F, Sun Y. *Nat Commun*, 2020, 11: 2855
26 Wu Q, Wang W, Wu Y, Chen Z, Guo J, Sun R, Guo J, Yang YM, Min J. *Adv Funct Mater*, 2021, 31: 2010411
27 Wang Y, Zhu Q, Naveed HB, Zhao H, Zhou K, Ma W. *Adv Energy Mater*, 2020, 10: 1903609
28 Sun R, Wu Q, Guo J, Wang T, Wu Y, Qiu B, Luo Z, Yang W, Hu Z, Guo J, Shi M, Yang C, Huang F, Li Y, Min J. *Joule*, 2020, 4: 407–419
29 Fan Q, Fu H, Luo Z, Oh J, Fan B, Lin F, Yang C, Jen AKY. *Nano*

*Energy*, 2022, 92: 106718
30 Liu T, Yang T, Ma R, Zhan L, Luo Z, Zhang G, Li Y, Gao K, Xiao Y, Yu J, Zou X, Sun H, Zhang M, Dela Peña TA, Xing Z, Liu H, Li X, Li G, Huang J, Duan C, Wong KS, Lu X, Guo X, Gao F, Chen H, Huang F, Li Y, Li Y, Cao Y, Tang B, Yan H. *Joule*, 2021, 5: 914–930
31 Fu H, Li Y, Yu J, Wu Z, Fan Q, Lin F, Woo HY, Gao F, Zhu Z, Jen AKY. *J Am Chem Soc*, 2021, 143: 2665–2670
32 Shan T, Hong Y, Zhu L, Wang X, Zhang Y, Ding K, Liu F, Chen CC, Zhong H. *ACS Appl Mater Interfaces*, 2019, 11: 42438–42446
33 Kim YJ, Park CE. *APL Mater*, 2015, 3: 126105
34 Pfadler T, Coric M, Palumbiny CM, Jakowetz AC, Strunk KP, Dorman JA, Ehrenreich P, Wang C, Hexemer A, Png RQ, Ho PKH, Müller-Buschbaum P, Weickert J, Schmidt-Mende L. *ACS Nano*, 2014, 8: 12397–12409
35 Sun H, Liu T, Yu J, Lau TK, Zhang G, Zhang Y, Su M, Tang Y, Ma R, Liu B, Liang J, Feng K, Lu X, Guo X, Gao F, Yan H. *Energy Environ Sci*, 2019, 12: 3328–3337
36 Cheng P, Wang R, Zhu J, Huang W, Chang SY, Meng L, Sun P, Cheng HW, Qin M, Zhu C, Zhan X, Yang Y. *Adv Mater*, 2018, 30: 1705243
37 Guo H, Yang CY, Zhang X, Motta A, Feng K, Xia Y, Shi Y, Wu Z, Yang K, Chen J, Liao Q, Tang Y, Sun H, Woo HY, Fabiano S, Facchetti A, Guo X. *Nature*, 2021, 599: 67–73
38 Zhao Y, Liu T, Wu B, Zhang S, Prine N, Zhang L, Pang S, Yin B, Ye L, Gu X, Yu G, Duan C, Huang F, Cao Y. *Chem Mater*, 2021, 33: 3746–3756
39 Ma R, Yu J, Liu T, Zhang G, Xiao Y, Luo Z, Chai G, Chen Y, Fan Q, Su W, Li G, Wang E, Lu X, Gao F, Tang B, Yan H. *Aggregate*, 2021, e58
40 Qiu B, Chen Z, Qin S, Yao J, Huang W, Meng L, Zhu H, Yang YM, Zhang ZG, Li Y. *Adv Mater*, 2020, 32: 1908373
41 Chen Z, Chen X, Jia Z, Zhou G, Xu J, Wu Y, Xia X, Li X, Zhang X, Deng C, Zhang Y, Lu X, Liu W, Zhang C, Yang YM, Zhu H. *Joule*, 2021, 5: 1832–1844
42 Selvin PR, Rana TM, Hearst JE. *J Am Chem Soc*, 1994, 116: 6029–6030
43 Lin Y, Zhao F, Prasad SKK, Chen JD, Cai W, Zhang Q, Chen K, Wu Y, Ma W, Gao F, Tang JX, Wang C, You W, Hodgkiss JM, Zhan X. *Adv Mater*, 2018, 30: 1706363
44 Qin J, Chen Z, Bi P, Yang Y, Zhang J, Huang Z, Wei Z, An C, Yao H, Hao X, Zhang T, Cui Y, Hong L, Liu C, Zu Y, He C, Hou J. *Energy Environ Sci*, 2021, 14: 5903–5910
45 Liao Q, Wang Y, Yao X, Su M, Li B, Sun H, Huang J, Guo X. *ACS Appl Mater Interfaces*, 2021, 13: 16744–16753
46 Murgatroyd PN. *J Phys D-Appl Phys*, 1970, 3: 151–156
47 Kang Q, Zheng Z, Zu Y, Liao Q, Bi P, Zhang S, Yang Y, Xu B, Hou J. *Joule*, 2021, 5: 646–658
48 Cowan SR, Roy A, Heeger AJ. *Phys Rev B*, 2010, 82: 245207